

Article

Neck Structure Optimal Design of the Turbine Wheel for Containment Design of the Air Turbine Starter

Liqiang Chen ¹, Haijun Xuan ^{2,*}, Wenbin Jia ², Jianxin Liu ³, Zehui Fang ⁴ and Yao Zheng ¹ ¹ School of Aeronautics and Astronautics, Zhejiang University, Hangzhou 310027, China² College of Energy Engineering, Zhejiang University, Hangzhou 310027, China³ AECC Hunan Aviation Powerplant Research Institute, Zhuzhou 412002, China⁴ Zhejiang HIRO Aeronautics Technology Co., Ltd., Huzhou 313219, China

* Correspondence: marine@zju.edu.cn

Abstract: The airworthiness standards of the transport category airplanes stipulate that the high energy rotor equipment must be of the sufficient containment capacity. It is of great importance to study the containment and weight reduction for the air turbine starter. In this paper, based on an OSF design, Kriging response surface model and MOGA algorithm, a neck structure optimal design method was proposed for the air turbine wheel. Using the optimal design method, the optimal structural parameters were suggested as the design parameters, and verified by the over-speed burst test. The maximum errors of the burst speeds between the experimental and design values are less than 2%, and the neck structure turbine wheel breaks in the neck as expected, validating the accuracy of the optimal design method. Then, the effects of turbine wheel burst modes on the containment were investigated quantitatively, and verified by the containment tests. Based on the experimental and simulation results, the containment design method was proposed for the neck structure turbine wheel. The results show that compared with the trisection wheel burst, the rim burst dramatically decrease the mass and initial kinetic energy of burst released fragments by 63.3% and 24.8%, thereby greatly reducing the thickness and the mass of the containment ring by 29.5% and 29.1%.



Citation: Chen, L.; Xuan, H.; Jia, W.; Liu, J.; Fang, Z.; Zheng, Y. Neck Structure Optimal Design of the Turbine Wheel for Containment Design of the Air Turbine Starter. *Aerospace* **2023**, *10*, 802. <https://doi.org/10.3390/aerospace10090802>

Academic Editor: Zhongqing Su

Received: 17 July 2023

Revised: 12 September 2023

Accepted: 12 September 2023

Published: 14 September 2023



Copyright: © 2023 by the authors. Licensee MDPI, Basel, Switzerland. This article is an open access article distributed under the terms and conditions of the Creative Commons Attribution (CC BY) license (<https://creativecommons.org/licenses/by/4.0/>).

Keywords: air turbine starter; wheel containment; containment ring; neck structure turbine wheel; optimal design method; containment design method

1. Introduction

Due to the light weight and high power, the air turbine starter is the best choice used to start an aero engine, and has been widely used in aircraft [1]. The working speed of the air turbine starter is always above 60,000 rpm, which means that the turbine wheel has a high kinetic energy [2]. Therefore, a serious aviation accident will occur once the turbine wheel breaks [3]. In October 2007, the turbine wheel of the air turbine starter of an A330-300 aircraft broke, and the broken wheel pieces damaged the integrated drive generator [4]. In October 2013, the turbine wheel of the air turbine starter of an A330-302 aircraft broke, and the broken wheel pieces damaged the oil pipeline [5]. By 2007, for the CFM International turbofan engines-CFM56 series, several in-service uncontained failures of the air turbine starter had resulted in damage to the engine and fan cowl [6]. Therefore, it is of great importance to realize the containment of the turbine wheel for an air turbine starter.

The airworthiness standards of the United States (FAR 25.1461) [7] and China (CCAR 25.1461) [8] demand that high energy rotor equipment must be of sufficient containment capacity. Therefore, several researchers have studied the containment design method of the turbine wheel. Martino [9] experimentally researched the containment for bisection, trisection and quarter wheel burst, and analysed the effect of the number of broken wheel pieces on the containment. McCallum [10] studied the containment for the trisection wheel

burst by simulation and test, and found that shear failure occurred in the impact zone of the containment ring. Collins [11] used the collision-imparted method (CIVM) to predict the containment process of the containment casing for a trisection wheel. Hagg [12] experimentally investigated the containment of a steel cylindrical shell for missile-like steel wheel pieces, and illustrated the containment process for the quarter wheel pieces. Gerstle [13] proposed an analytical simulation technique based on large deflection theory and finite difference numerical methods, and predicted the containment process of an orthogonally woven fabric shield. In 1984, Giard [14] researched the relationship between the number of the broken wheel pieces and the translational energy per piece. The research result shows that the trisection wheel burst results in the maximum translational energy per piece, therefore, the containment of a trisection wheel burst has been mostly studied since then. For the T53-L-13L engine of the UH-1 Huey helicopter, Frankenberger [15] conducted the containment test to demonstrate the containment capability of the containment ring for the trisection turbine wheel burst. Teng [16] numerically studied the failure response of the 2219-T851 aluminium containment panel, which was obliquely impacted by the titanium turbine wheel piece. Stamper [17] considered the effects of the material model, mesh density and element formulation on the simulation results, and developed a method by using ANSYS/LS-DYNA to predict the containment process. Then he simulated the containment process to verify the accuracy and reliability of the developed method. Carney [18] experimentally analysed a fan blade containment system with an alternate geometry to reduce jet engine weight. Li [19] simulated the process of a trisection wheel piece impacting on single and double-layered plates to determine the optimal structure of the aero-engine casing. Xuan [20] studied the containment of the aero-engine casing for the trisection wheel burst by the simulation and test, and illustrated the process of the wheel pieces impacting on the aero-engine casing. Winter [21] used the explicit finite element technique to research the containment process of the compressor housing for the trisection wheel burst, and the simulation results were in conformity to the test results. However, there are few studies on the containment of the air turbine starter.

Giard [8] investigated the containment of the air turbine starter, and proposed the design method of the containment ring. The research result shows that the best combination of ultimate tensile strength and elongation results in the best theoretical energy absorption and lightest weight design. Bai [22] researched the containment of the U type containment ring for the three-piece wheel burst by the simulation and test, and designed the groove depth of the U type containment ring. However, the above research focuses on the design method of the containment ring.

There are two methods to realize the containment of the turbine wheel for an air turbine starter. One method is that the containment ring is designed to meet the containment capacity. The other method is that the neck structure turbine wheel is designed to realize the rim burst, and the impact energy of the burst pieces is reduced to meet the containment capacity. However, there are few investigations for the design method of the neck structure turbine wheel. Therefore, a neck structure optimal design of the turbine wheel for the containment design of the air turbine starter was first proposed in this paper. The results of this study can be used to optimize the containment of in-service air turbine starters and to design the containment of new air turbine starters, which has great engineering application value.

The neck structure turbine wheel of the air turbine starter is shown in Figure 1, and the remainder of this paper can be summarized as follows. In Section 2, a neck structure optimal design method was proposed for the turbine wheel, and the design parameters of the neck structure turbine wheel were given. In Section 3, the rotor over-speed burst tests were conducted to verify the optimal design method. In Section 4, the effect of turbine wheel burst modes on the containment was investigated quantitatively by the simulation. In Section 5, the containment tests were conducted for the trisection wheel burst and rim burst to verify the simulation results of Section 4. Based on the experimental and simulation

results, the containment design method was proposed for the neck structure turbine wheel. In Section 6, some key conclusions of this work are summarized.

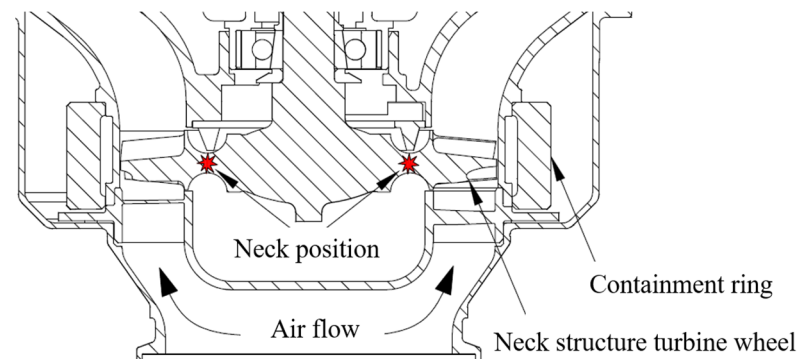


Figure 1. Neck structure turbine wheel of the air turbine starter.

2. A Neck Structure Optimal Design Method for the Turbine Wheel

A neck structure optimal design method for the turbine wheel was proposed, as shown in Figure 2. Step 1: first, the parametric model of the neck structure turbine wheel is established, and six structural parameters are selected to be optimized. Step 2: FEM simulation is conducted. Step 3: afterwards, three target parameters are selected, and the optimization objective is set. Step 4: the uniform sample database is generated by the optimal space-filling (OSF) design. Step 5: the Kriging response surface model is then established to characterize the relationship between the target and structure parameters. Step 6: the optimal solution is solved by the multi-objective genetic algorithm (MOGA), and the optimized structural parameters are obtained. Step 7: FEM simulation is conducted for the neck structure turbine wheel with the optimized structural parameters, and the simulation results of the target parameters are obtained. Step 8: last, the simulation results and optimization objectives are compared. If the simulation results meet the optimization objectives, the optimization is finished; otherwise, the sample size is increased, and Steps 4 to 7 are repeated until the simulation results meet the optimization objectives.

2.1. Parametric and Finite Element Model

To improve optimization efficiency, the parametric model of the neck structure turbine wheel is carried out. Twelve structure parameters ($L1-L11$ and $\theta1$) at the neck for the turbine wheel are shown in Figure 3. $L1$, $L2$, $L3$, $L4$ and $L5$ are the same length as $L10$, $L9$, $L8$, $L7$ and $L6$, respectively. $L11$ is the minimum distance at the neck, and $\theta1$ is the angle between $L3$ and $L8$. Therefore, six structure parameters ($L1$, $L2$, $L4$, $L5$, $L11$ and $\theta1$) are selected to be optimized as $P1-P6$, as shown in Figure 3.

To reduce the calculation cost, the finite element model of the neck structure turbine wheel with two straight blades is established, as shown in Figure 4. The blade shape has great effect on the aerodynamic performance, but has little effect on the containment of turbine wheel. Therefore, the real blades are replaced by the straight blades, and the rotational inertia of the wheel with the straight blades is same as that with the real blades. The neck structure turbine wheel is meshed by the tetrahedral solid element. The mesh sizes of the blades, the neck part and central part of the wheel are 0.5 mm, 0.5 mm and 1 mm, respectively. The end surface is constrained in displacement in the axial and radial directions. The two radial sections are constrained in displacement in the circumferential direction. Titanium alloy TC4 (in Chinese) is chosen for the turbine wheel, and the material parameters are listed in Table 1. The bilinear elastic–plastic material model is adopted, and the tangent modulus is 1886 MPa.

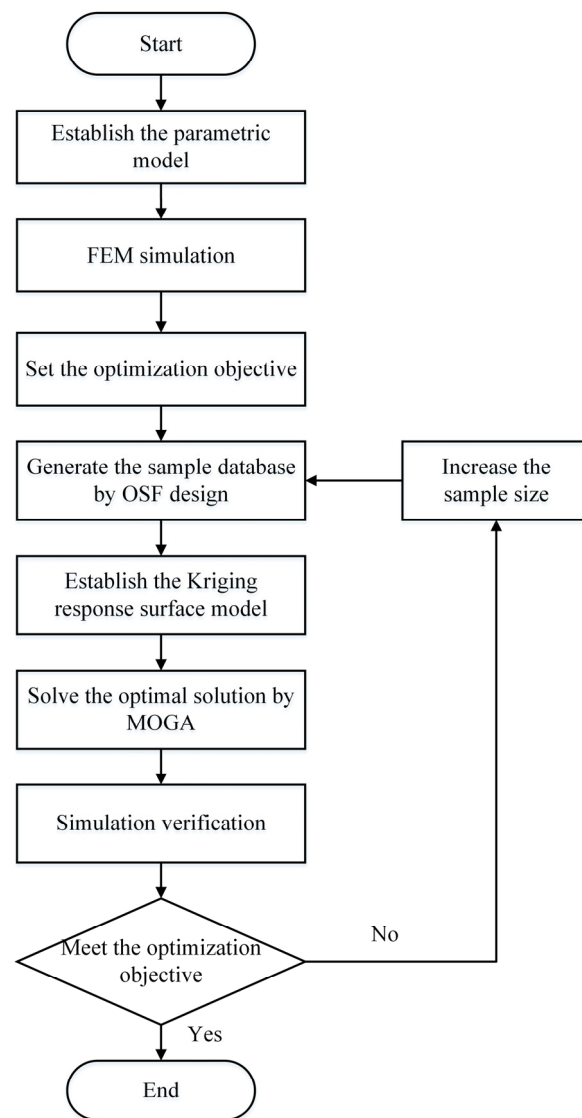


Figure 2. Neck structure optimal design method for the turbine wheel.

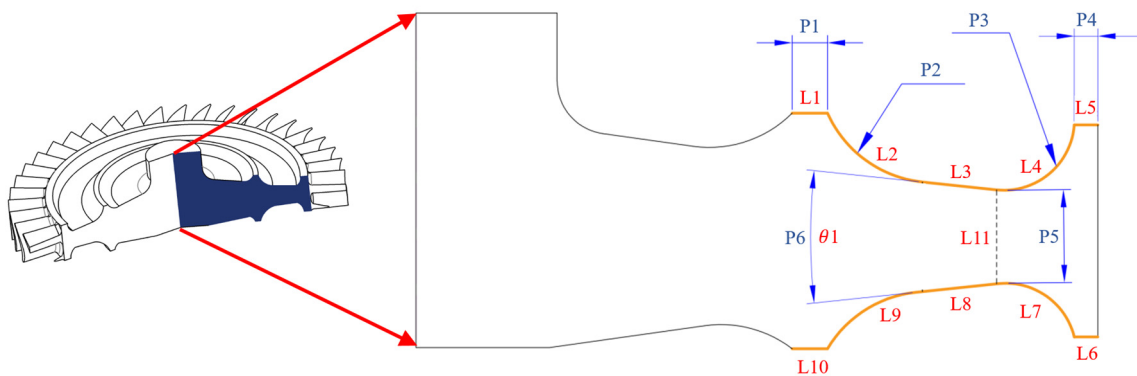


Figure 3. Structure parameters at the neck for the turbine wheel.

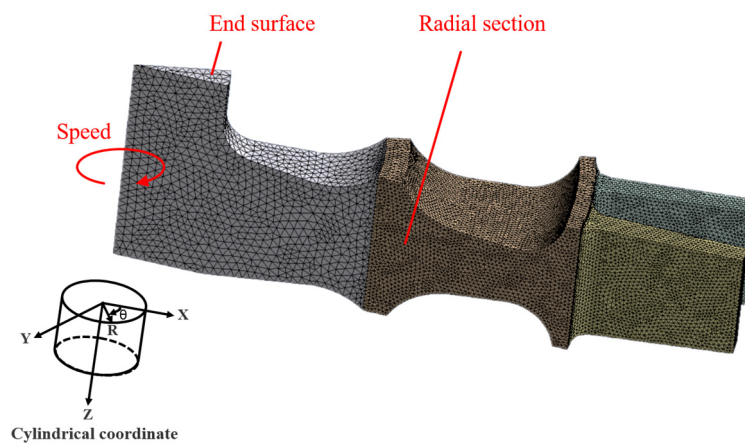


Figure 4. Finite element model of the neck structure turbine wheel.

Table 1. Material parameters of TC4.

Parameters	Value
Density ρ (kg/m ³)	4440
Elastic modulus (GPa)	110
Poisson's ratio	0.33
Yield strength (MPa)	825
Tensile strength (MPa)	985
Elongation (%)	10

In the condition of the clutch connect failure, the air turbine starter may experience operation at a turbine free run speed, in which the turbine wheel operates without a resistive load on the output shaft, causing the turbine to accelerate to a high speed. To ensure the turbine wheel does not burst at the turbine free run speed, the safety margin is design as 1.15 by considering the material property dispersion, machining error and operation temperature of the turbine wheel. For a certain type of air turbine starter, the turbine free run speed is 78,000 r/min, and the burst speed is designed as 89,700 r/min (1.15 times the turbine free run speed). Therefore, the rotating speed is set to 89,700 r/min here for the burst speed calculation.

2.2. Optimization Objective

To break the turbine wheel at the neck, the maximum radial stress $\sigma_{r-\max}$ at the target speed should reach the tensile strength σ_b , while the maximum circumferential stress $\sigma_{c-\max}$ and maximum equivalent stress $\sigma_{Mises-\max}$ are less than σ_b . Therefore, $\sigma_{r-\max}$, $\sigma_{c-\max}$ and $\sigma_{Mises-\max}$ are selected as target parameters P7 to P9, and the optimization objective is set as:

$$\begin{cases} \sigma_{r-\max} = \sigma_b \\ \sigma_{c-\max} < \sigma_b \\ \sigma_{Mises-\max} < \sigma_b \end{cases} \quad (1)$$

When the maximum radial stress reaches the tensile strength, the smaller the maximum circumferential stress is, the easier it is to control the turbine wheel breaks at the neck cylindrical section. Therefore, a scaling factor $\lambda = \sigma_{r-\max} / \sigma_{c-\max}$ is introduced. Without loss of generality, the value of λ starts from 1.1, and increases by 0.1 (i.e., 1.1, 1.2, 1.3, 1.4, 1.5,) until the optimal solution cannot be solved.

2.3. Optimization Process

The optimization process flowchart is shown in Figure 5. First, the design variables (P1–P6) and variation range that need to be optimized are defined, and the parametric

modelling is carried out. Then, FEM simulation is conducted and the target parameters (P7–P9) are selected. The sample database, which consists of P1 to P9, is generated by using the OSF design method. Based on the sample database, the Kriging response surface model is established to obtain the relationship between the target parameters (P7–P9) and structure parameters (P1–P6). Then, the optimization objective and constraints are set. At last, the optimal structural parameters are obtained by using the MOGA after 100 iterations.

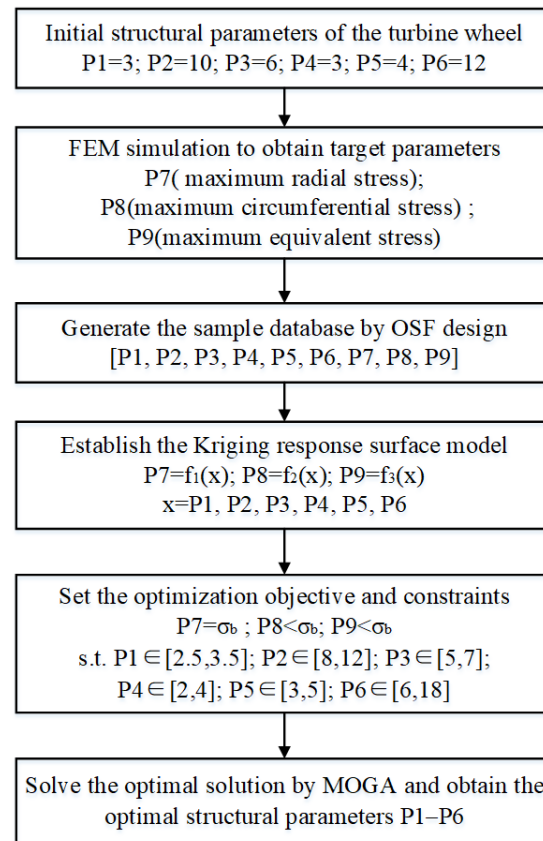


Figure 5. Optimization process flowchart.

The initial value and variation range of the structural parameters are listed in Table 2. The closer to the rim, the greater the centrifugal force. In addition, the structural parameters close to the wheel rim (P3, P4 and P5) have a greater effect on the target parameters than the structural parameters far from the wheel rim (P1). Therefore, the variation ranges of P3, P4 and P5 are set to 2 mm, while that of P1 is set as 1 mm. The larger variation ranges of P2 and P6 (4 mm and 12°) are set to ensure the optimal structure can be formed.

Table 2. Initial value and variation range of the structural parameters.

Parameters	Initial Value	Variation Range
P1 (mm)	3	2.5–3.5
P2 (mm)	10	8–12
P3 (mm)	6	5–7
P4 (mm)	3	2–4
P5 (mm)	4	3–5
P6 (°)	12	6–18

The OSF design and Kriging response surface model have a high precision for multi-dimensional integration problems [23,24]. Six structural parameters (P1–P6) need to be optimized, therefore, the OSF design and Kriging response surface model are adopted.

The Kriging approximate model is a model based on structural analysis and variogram theory to perform unbiased optimal estimation of regionalized variables in a limited region, and can be used to solve problems with a high degree of nonlinearity to obtain the ideal fitting effect [24]. This method is suitable in the case of a small sample point disturbance, and the calculation speed of this algorithm is faster than other methods. Compared with other approximate models such as nonlinear regression, neural network and sparse grid, the Kriging approximate model is used in fewer occasions and corresponds to the corresponding sample point generation methods. Since the data points in the OSF sample library need to be calculated by finite elements and evaluated by error, the results of the sample library have a high accuracy. It means that compared with the fitting method, the interpolation method is better, so the Kriging method is adopted to generate the response surfaces.

To ensure the precision of the calculation, the fourth-order polynomial is adopted for the Kriging response surface model. The minimum sample number of the fourth-order model can be determined by [25]:

$$K_{\min} = \frac{(N+1)(N+2)}{2} + 2N \quad (2)$$

where the number of optimized parameters is $N = 6$.

The minimum sample number $K_{\min} = 40$, therefore, 45 samples are selected for the Kriging response surface model. The sample number of OSF design depends on that of the Kriging response surface model, therefore, 45 samples are selected for the OSF design. According to Table 2, a uniform sample database with 45 samples is generated by employing the OSF design, and every sample includes six structural parameters (P1–P6) and three target parameters (P7–P9), as list in Table 3.

Table 3. Sample database generated by the OSF design.

No.	P1 (mm)	P2 (mm)	P3 (mm)	P4 (mm)	P5 (mm)	P6 (°)	P7 (MPa)	P8 (MPa)	P9 (MPa)
1	2.82	8.40	6.04	2.91	4.76	16.80	910	620	806
2	2.89	10.18	6.49	3.80	4.04	6.13	913	687	837
3	2.51	10.44	6.44	2.38	4.62	11.20	886	620	794
4	2.58	9.73	5.96	2.64	3.60	6.67	942	693	839
5	2.93	11.51	5.02	2.69	3.56	13.33	838	677	843
6	3.29	8.93	5.42	2.56	4.93	10.93	697	600	756
7	2.91	10.89	5.91	2.02	3.20	10.13	958	725	839
8	3.40	9.38	5.24	2.96	4.13	17.07	827	642	845
9	3.04	11.16	5.73	3.31	4.84	17.33	919	619	811
10	2.56	11.42	5.51	3.27	4.18	7.73	904	655	843
11	2.64	9.64	5.47	3.98	4.44	13.07	956	656	843
12	2.78	8.58	6.93	2.87	4.27	9.33	932	659	840
13	3.00	8.22	6.67	2.60	3.64	16.00	998	690	838
14	3.27	11.78	6.40	3.36	3.24	12.80	1030	776	862
15	2.76	10.27	6.58	2.73	3.02	15.47	1076	798	871
16	3.13	8.84	5.20	3.09	3.11	13.60	1024	740	841
17	3.24	10.62	5.16	3.67	4.67	10.67	865	636	830
18	3.31	10.00	5.87	2.42	3.33	17.60	968	691	837
19	2.87	11.60	6.98	2.78	3.69	9.87	973	689	837
20	2.53	11.07	5.60	3.00	3.78	15.73	942	669	839
21	3.42	9.02	6.62	2.82	4.49	8.00	929	642	828
22	3.38	11.24	6.09	3.40	3.96	6.40	973	672	839
23	3.47	10.80	6.76	2.29	3.82	12.00	972	660	840
24	2.80	8.76	5.78	3.13	4.89	8.27	861	622	788
25	2.62	9.29	6.89	3.76	3.87	14.13	888	708	837
26	2.73	8.67	6.00	3.62	3.07	11.73	1049	845	883
27	3.36	11.87	5.64	2.51	4.40	12.53	790	623	816

Table 3. Cont.

No.	P1 (mm)	P2 (mm)	P3 (mm)	P4 (mm)	P5 (mm)	P6 (°)	P7 (MPa)	P8 (MPa)	P9 (MPa)
28	3.44	9.11	6.36	3.49	3.29	10.40	1015	787	861
29	2.67	8.13	5.07	3.04	3.91	12.27	823	661	842
30	2.69	11.33	6.22	3.84	3.38	11.47	994	774	856
31	3.49	10.09	5.38	2.47	3.47	8.53	889	697	842
32	3.22	8.49	5.82	3.89	4.31	14.93	948	659	843
33	3.11	10.71	5.33	3.93	3.51	15.20	1044	715	841
34	3.07	8.31	6.27	2.33	3.42	8.80	977	704	841
35	2.84	11.69	6.31	2.24	4.36	16.53	914	625	825
36	2.71	10.98	6.80	3.58	4.71	14.67	854	642	837
37	3.33	9.82	6.71	3.71	3.73	16.27	918	712	835
38	3.18	9.91	6.13	2.20	4.53	17.87	854	612	799
39	3.09	10.53	6.53	2.11	4.58	7.47	829	616	782
40	2.98	11.96	6.18	3.18	4.98	9.60	883	614	786
41	2.96	9.56	5.11	2.16	4.22	9.07	727	671	802
42	2.60	9.20	5.56	2.07	4.09	14.40	758	657	832
43	3.16	8.04	5.69	3.53	4.00	7.20	956	677	842
44	3.02	10.36	5.29	3.22	3.16	6.93	1013	782	854
45	3.20	9.47	6.84	3.44	4.80	13.87	851	636	830

The Kriging response surface model is established to characterize the relationship between the target parameters and structure parameters, and can be expressed as:

$$f(x) = y(x) + z(x) \quad (3)$$

where $f(x)$ are the object functions (i.e., three target parameters P7–P9), $y(x)$ are the fourth-order polynomial functions correspondence with six structural parameters (P1–P6) and $z(x)$ is the deviation of the results between the Kriging response surface model and FEM simulation.

MOGA [26] is a multi-objective iterative genetic algorithm, which sorts all individuals in a population based on the basic principle of Pareto Optimality, and carries out selection operations in the evolution process on the arranged order. This will make the first Pareto best individuals have a greater probability of inheriting to the next generation. After many algebraic cycles, the optimal Pareto solution of multi-objective optimization problem can be finally obtained. This method is suitable for multi-objective optimization problems, the optimal design of global search and the response surface model. Therefore, MOGA is adopted in this paper.

Based on the Kriging response surface model, the optimal solution (the optimized structural parameters) is solved by employing the MOGA algorithm to meet the optimization objective. In addition, the optimized structural parameters (P1–P6) are obtained as listed in Table 4. It should be noted that when $\lambda > 1.5$, the optimal solution cannot be solved, which means that no turbine wheel structure can make λ greater than 1.5.

Table 4. Optimized structural parameters.

Parameters	$\lambda = 1.1$	$\lambda = 1.2$	$\lambda = 1.3$	$\lambda = 1.4$	$\lambda = 1.5$	$\lambda = 1.6$
P1 (mm)	2.74	3.49	2.62	3.01	3.35	-
P2 (mm)	9.01	10.86	10.95	11.68	11.66	-
P3 (mm)	6.37	6.83	6.65	6.27	6.74	-
P4 (mm)	3.89	3.47	3.25	3.66	2.30	-
P5 (mm)	3.01	3.13	3.44	3.66	3.75	-
P6 (°)	9.80	14.77	7.80	14.00	13.36	-

2.4. Sensitivity Analysis

To study the effect of the structural parameters on the target parameters, a sensitivity analysis between the target and structural parameters was conducted. The sensitivities of six structural parameters on the maximum radial and circumferential stress ($\sigma_{r-\max}$ and $\sigma_{c-\max}$) are shown in the Figure 6. Figure 6 shows that the sensitivities of P5 on $\sigma_{r-\max}$ and $\sigma_{c-\max}$ (0.776 and 0.945) are the maximum, which means that the minimum distance at the neck effects most on the target parameters. Figure 6 also shows that the sensitivities of P3, P4 and P5 are larger than 0.1, whereas that of P1, P2 and P6 are less than 0.08. It means that the structural parameters close to the wheel rim have a greater effect on the target parameters than the structural parameters far from the wheel rim. The results verify the rationality of variation range of the structural parameters in Section 2.3.

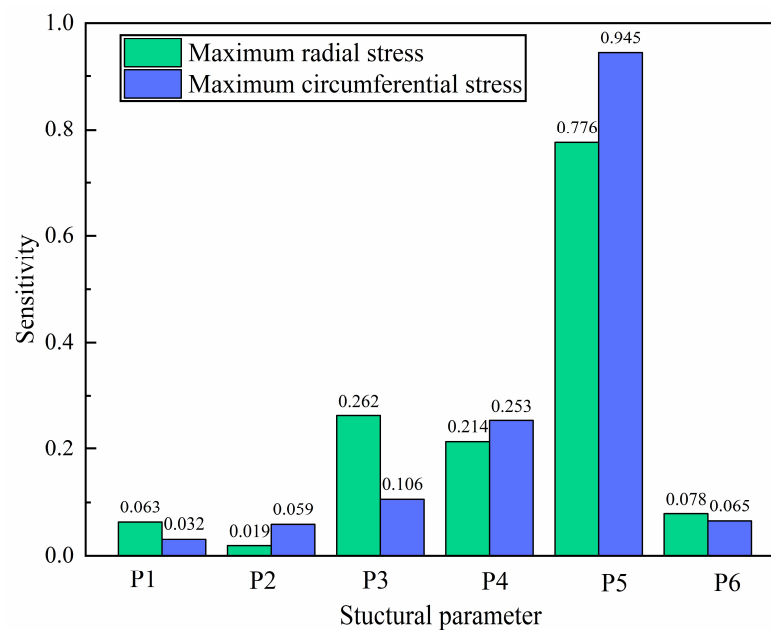


Figure 6. Sensitivities of the structural parameters on the target parameters.

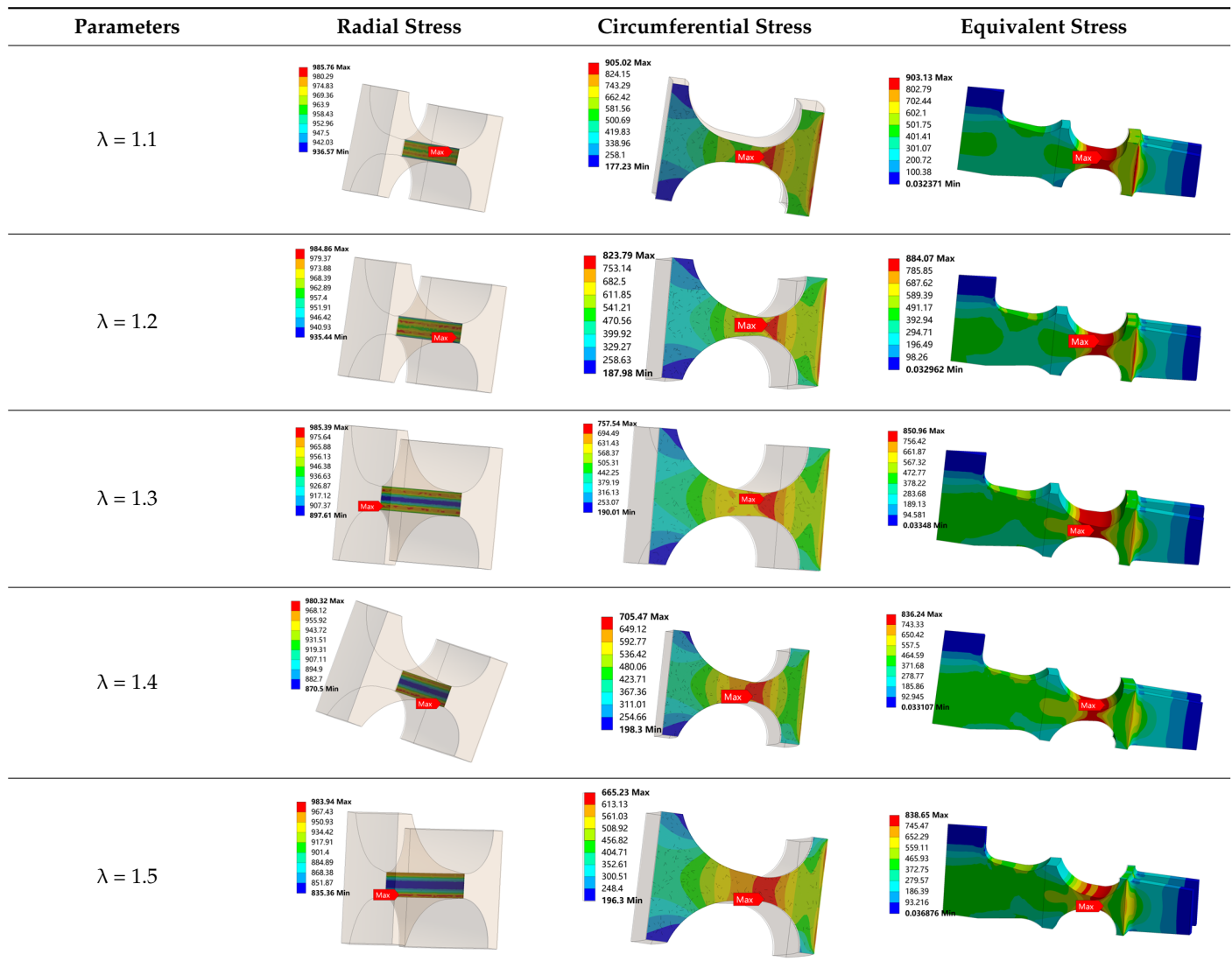
2.5. Simulation Verification

According to Equation (3), a deviation exists between the Kriging response surface model and FEM simulation, therefore, the FEM simulation needs to be conducted to verify the optimized structural parameters. According to the optimized structural parameters, FEM simulation is conducted and the simulation results are shown in Tables 5 and 6. Table 5 is simulation result of the target parameters. Table 5 shows that P8 and P9 are less than σ_b , and the errors of P7 are less than 1.5%. It means that the target parameters meet the optimization objective (Equation (1)), which verifies the optimized structural parameters in Table 4. Table 6 is the stress distribution of the turbine wheel. Table 6 shows that when $\lambda = 1.1$, the radial stress at the neck is 986 MPa, which reaches the tensile strength σ_b . The circumferential stress and equivalent stress at the neck are 905 MPa and 903 MPa, which are less than the radial stress. It means that the turbine wheel with $\lambda = 1.1$ breaks in the neck along the circumferential direction. The stress distributions for $\lambda = 1.2, 1.3, 1.4$ and 1.5 are similar to $\lambda = 1.2$. Table 6 also shows that the maximum radial stress, circumferential stress and equivalent stress occur at the neck, which proves the correctness of the simulation results.

Table 5. Simulation results of the target parameters.

Parameters	$\lambda = 1.1$	$\lambda = 1.2$	$\lambda = 1.3$	$\lambda = 1.4$	$\lambda = 1.5$
P7 (MPa)	986	985	985	980	984
P8 (MPa)	905	824	758	705	665
P9 (MPa)	903	884	851	836	839

Table 6. Stress distribution of the turbine wheel.



It should be noted that the larger λ is, the more easily the turbine wheel breaks at the neck. However, a turbine wheel structure with a large λ is hard to process. Considering the processing cost, the optimized structural parameters for $\lambda = 1.2, 1.3$ and 1.4 can be adopted as design parameters.

3. Experimental Verification of the Optimal Design Method

To verify the optimal design method, three neck structure turbine wheels ($\lambda = 1.2, 1.3$ and 1.4) were processed, and disk burst tests were conducted.

3.1. Neck Structure Turbine Wheel

The practicality picture of the neck structure turbine wheel is shown in Figure 7. The cross-section and structural parameters of three turbine wheels ($\lambda = 1.2, 1.3$ and 1.4) are shown in Figure 3 and Table 4, respectively. The material parameters of the turbine wheel are listed in Table 1.



Figure 7. Practicality picture of the neck structure turbine wheel.

3.2. Rotor Over-Speed Burst Test

The disk burst tests are conducted on a high-speed spin tester, and the turbine wheel burst process is captured by a high-speed camera, as shown in Figure 8. The neck structure turbine wheel is driven by a spin shaft, which is powered by a drive shaft. The tester cavity is vacuumed to 2Torr by the vacuum pumps in order to avoid the air friction. The trigger wire is glued on the internal wall of the protective ring. As the wheel fragments cut off the trigger wire, the trigger signal will be sent to the control system to shut down the driver motor. Meanwhile, the high-speed camera is triggered to record data. The sample frequency of 51 kfps is set for the high-speed camera to ensure that the burst process is captured.

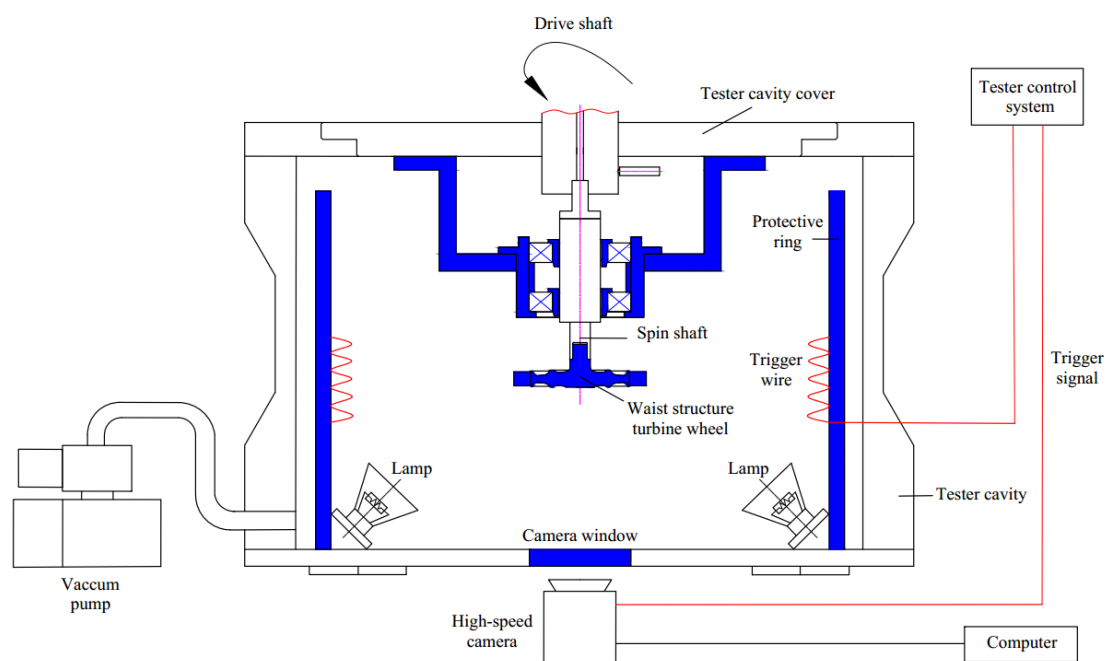


Figure 8. Rotor over-speed burst test system.

3.3. Comparison with Experimental Results

Figure 9 is the burst process of the neck structure turbine wheel with $\lambda = 1.2$. Figure 9 shows that when $t = 0$ ms, there is no crack in the wheel. When $t = 0.1$ ms, a circular arc crack appears in the neck of the wheel. The length and angle of the crack are one sixth of the circumference and 60° , respectively. When $t = 0.2$ ms, the crack expands along both the circumferential and radial directions. In the circumferential direction, the length and angle of the crack reach half of the circumference and 90° , respectively. In the radial direction, the crack splits the wheel rim in half. When $t = 0.3$ ms, the wheel rim is separated from the wheel, and breaks into five pieces. The burst processes for $\lambda = 1.3$ and 1.4 are similar to $\lambda = 1.2$, as shown in Figures 10 and 11. The experimental results illustrate that the neck structure turbine wheel breaks in the neck, which indicates the effectiveness of the optimal design method.

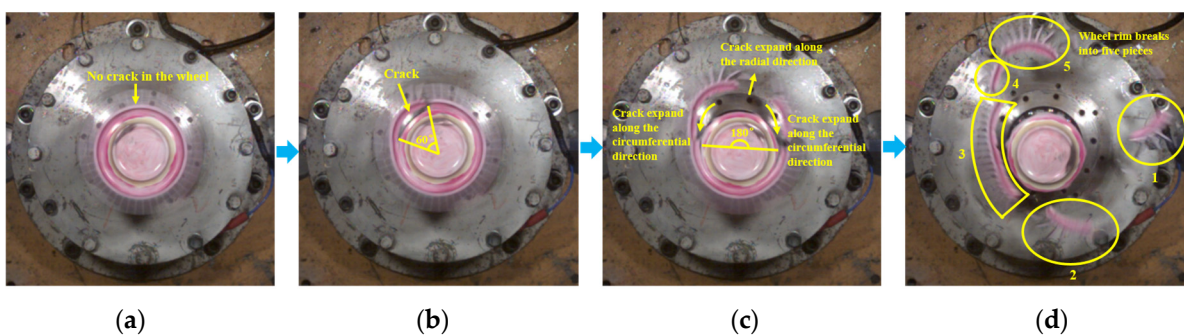


Figure 9. Burst process of the neck structure turbine wheel with $\lambda = 1.2$. (a) $t = 0$ ms; (b) $t = 0.1$ ms; (c) $t = 0.2$ ms; (d) $t = 0.3$ ms.

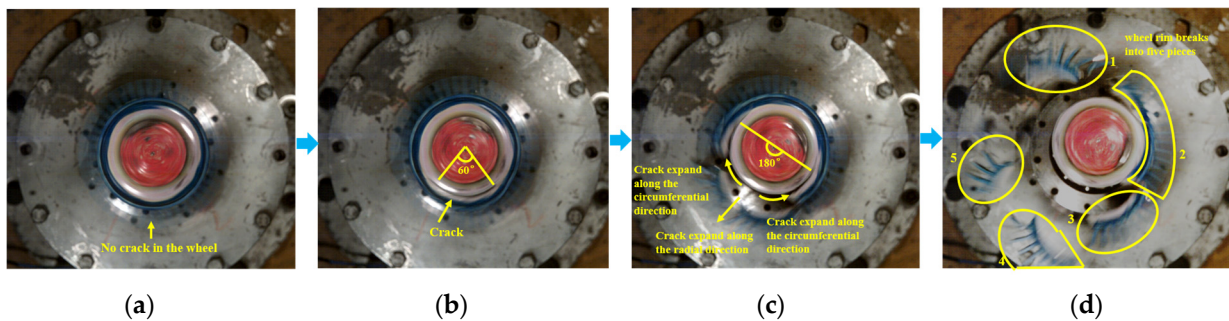


Figure 10. Burst process of the neck structure turbine wheel with $\lambda = 1.3$. (a) $t = 0$ ms; (b) $t = 0.1$ ms; (c) $t = 0.2$ ms; (d) $t = 0.3$ ms.

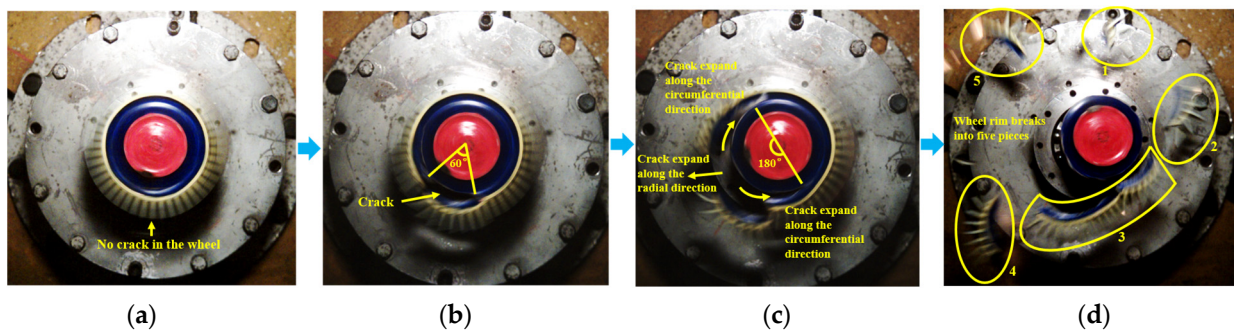


Figure 11. Burst process of the neck structure turbine wheel with $\lambda = 1.4$. (a) $t = 0$ ms; (b) $t = 0.1$ ms; (c) $t = 0.2$ ms; (d) $t = 0.3$ ms.

Figures 9d, 10d and 11d show that the wheel rim breaks into five pieces for the three neck structure turbine wheel, which means that the burst mode of the neck structure turbine wheel is a five piece burst of wheel rim. Figure 12 is the comparison of the masses and initial kinetic energies between the rim pieces and wheel. Figure 12a shows that compared with the wheel, the masses of the rim pieces for $\lambda = 1.2, 1.3$ and 1.4 decrease by 65.7%, 66.8% and 68.2%, respectively. Figure 12b shows that compared with the wheel, the initial kinetic energies of the rim pieces for $\lambda = 1.2, 1.3$ and 1.4 decrease by 22.0%, 23.4% and 24.7%, respectively. It means that the neck structure turbine wheel can dramatically decrease the mass and initial kinetic energy of the burst pieces from the wheel, thereby reducing the thickness and mass of the containment ring.

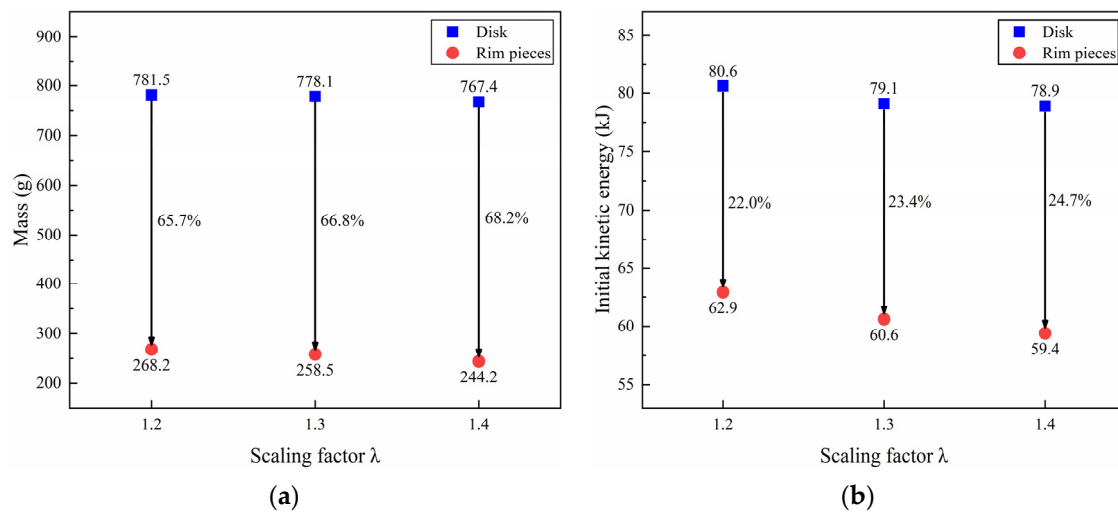


Figure 12. Comparison of the masses and initial kinetic energies between the rim pieces and wheel. (a) Descent rate of mass; (b) descent rate of initial kinetic energy.

Figure 13 is the comparison of the burst speed between the design and experimental values. Figure 13 shows that the errors of the burst speed for $\lambda = 1.2, 1.3$ and 1.4 are 1.2%, 1.0% and 0.68%, respectively. It indicates the accuracy of the optimal design method.

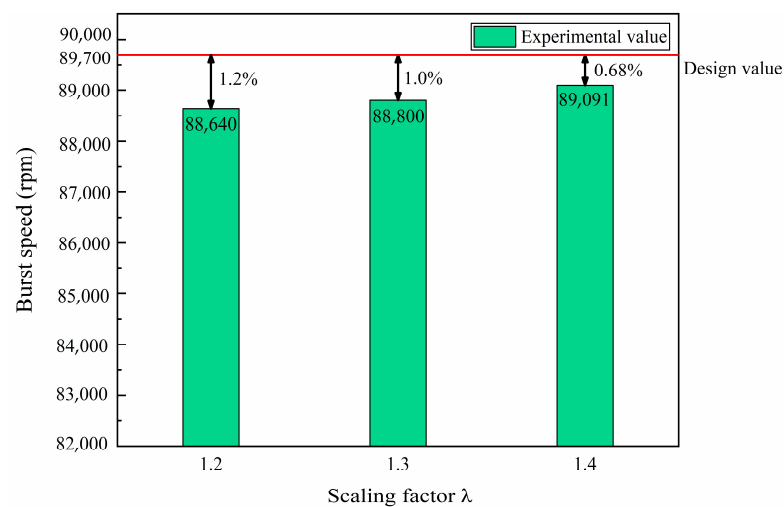


Figure 13. Comparison of the burst speed between the design and experimental values.

4. Effect of Turbine Wheel Burst Modes on Containment

According to Section 3.3, the rim burst of the turbine wheel can greatly reduce the requirement for the thickness of the containment ring. To quantitatively investigate the

effect of turbine wheel burst modes on the containment, the containment tests for different turbine wheel burst modes (the wheel burst and the rim burst) are simulated. The turbine wheel burst modes are shown in Figure 14.

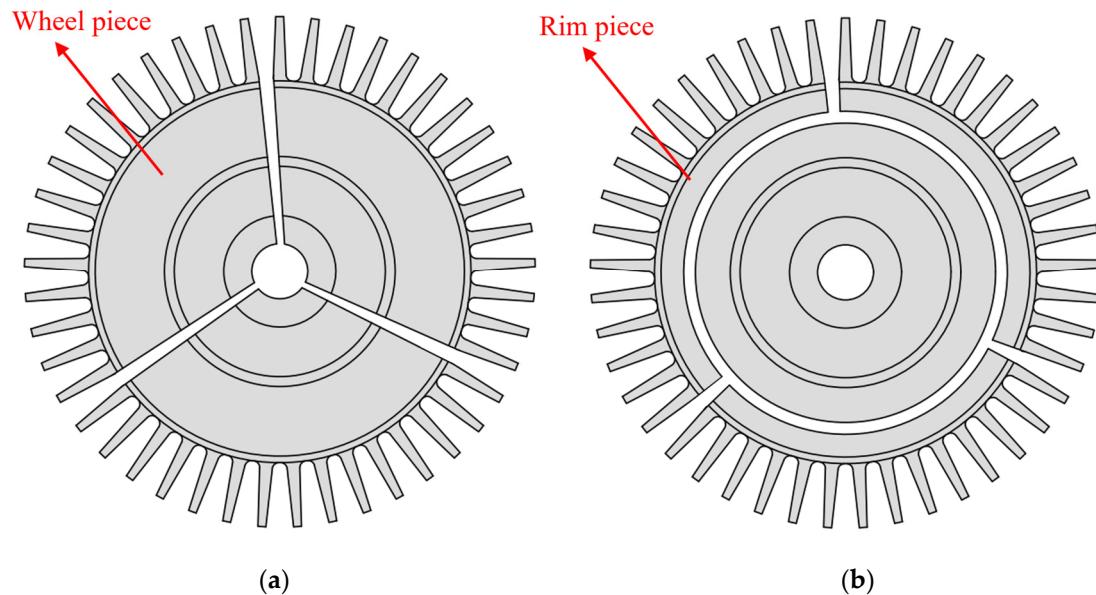


Figure 14. Turbine wheel burst modes. (a) Wheel burst; (b) rim burst.

Focusing on the wheel burst, the containment simulation for the trisection wheel burst is conducted, because the impact energy is at a maximum when the wheel is broken in three equal pieces [8]. Focusing on the rim burst, the containment simulations for the trisection, quarter and quintile rim burst are conducted. A trisection rim burst is investigated because the impact energy is at a maximum when the rim is broken in three equal pieces in the case of the rim burst. The quintile rim burst is investigated because the experimental results of the burst mode (as shown in Figures 9d, 10d and 11d) are a five piece burst of wheel rim. A quarter rim burst is studied for comparison.

4.1. Material Model

The containment ring and turbine wheel adopted the nickel-based alloy GH4169 and titanium alloy TC4, respectively. The Johnson–Cook (J-C) model [27,28] considers the effect of the strain rate on the material, and is therefore adopted for the containment ring and turbine wheel. The J-C model parameters of the two components are listed in Table 7. The detail information for the values of J-C model parameters can be found in our previous work [29].

Table 7. J-C model material parameters.

Material	A (MPa)	B (MPa)	n	C	M	D_1	D_2	D_3	D_4	D_5
GH4169	1180	1140	0.545	0.0134	1.3	0.11	0.24	1.92	0.00002	0.65
TC4	1089	1083	0.93	0.014	1.1	−0.09	0.27	0.48	0.014	3.87

4.2. Finite Element Model and Boundary Conditions

The finite element models of the turbine wheel, wheel rim and containment ring are shown in Figure 15. The geometric sizes of the neck structure for the turbine wheel and wheel rim are shown in Figure 3. The critical thicknesses of the containment ring for different turbine wheel burst modes are listed in Table 8.

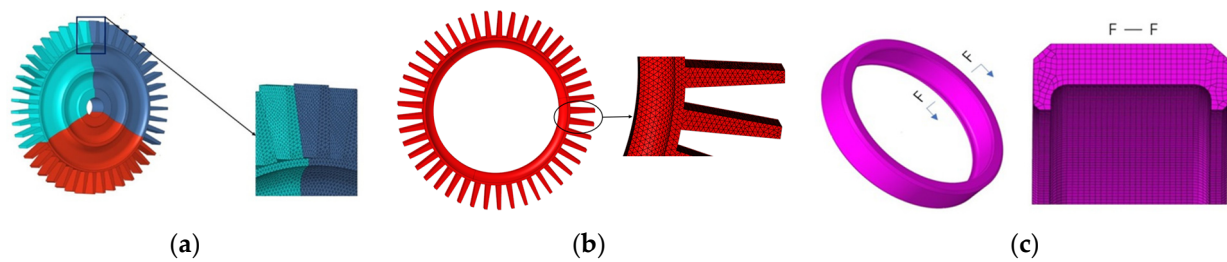


Figure 15. Finite element models. (a) Turbine wheel; (b) wheel rim; (c) containment ring.

Table 8. Thicknesses of the containment ring for different turbine wheel burst modes.

Burst Modes	Trisection Wheel Burst		Trisection Rim Burst		Quarter Rim Burst		Quintile Rim Burst	
Thickness Value (mm)	Critical 7.8	Comparison 7.6	Critical 5.5	Comparison 5.3	Critical 5.0	Comparison 4.8	Critical 4.0	Comparison 3.8

T denotes the thickness of the containment ring. To obtain the critical thickness, T is first estimated by the potential energy method [8] and then the containment simulation is conducted with the estimated thickness. If the containment ring breaks, the thickness is increased by 0.2 mm until the containment ring does not break; if the containment ring does not break, the thickness is decreased by 0.2 mm until the containment ring breaks. To verify the critical thickness of the containment ring, four thicknesses (0.2 mm less than the critical thickness) of the containment ring are taken for comparison, as listed in Table 8.

The turbine wheel and wheel rim are meshed by the tetrahedral solid element and the mesh size is 1 mm. The containment ring is meshed by the hexahedral solid element and the mesh size is 1 mm. The free boundary is adopted for the containment ring, which is consistent with the actual situation.

In the condition of the clutch disconnect failure, the air turbine starter is driven in reverse by the aeroengine and the experience operation at a higher speed (larger than the turbine free run speed). It leads to the failure of the support bearings, thus allowing axial travel of the turbine wheel. The turbine rim cutter is located in the air turbine starter, and the axial travel of the turbine wheel results in contact between the turbine wheel and the turbine rim cutter. For the contact position of the turbine wheel, the temperature sharply rises. It leads to the rapid reduction of the material property, thereby realizing the rim burst. The burst speed is designed as 1.05 times the turbine free run speed by considering the turbine bearing strength. For a certain type of the air turbine starter, the turbine free run speed is 78,000 r/min, so the burst speed is designed as 81,900 r/min (1.05 times the turbine free run speed).

4.3. Containment Simulation for the Wheel Burst

Figures 16 and 17 are the process of the turbine wheel pieces impacting the containment ring with $T = 7.8$ mm and $T = 7.6$ mm, respectively. Figure 16 shows that when $t = 0.09$ ms, the turbine wheel pieces first contact the containment ring, and the containment ring starts to deform. When $t = 0.30$ ms, the containment ring deforms plastically to absorb the impact energy, and its shape tends to be the triangular. When $t = 0.50$ ms, the turbine wheel pieces stop impacting the containment ring, and the containment ring fully deforms to be the triangle. Figure 17 shows that when $t = 0.09$ ms, the turbine wheel pieces first contact the containment ring, and the containment ring starts to deform. When $t = 0.15$ ms, the containment ring fully deforms plastically to be the triangle, but its absorbed energy is less than the impact energy of the turbine wheel pieces, and thereby the containment ring starts to break. When $t = 0.50$ ms, the containment ring breaks into three pieces. The simulation results illustrate that $T = 7.8$ mm is the critical thickness of the containment ring for the trisection wheel burst.

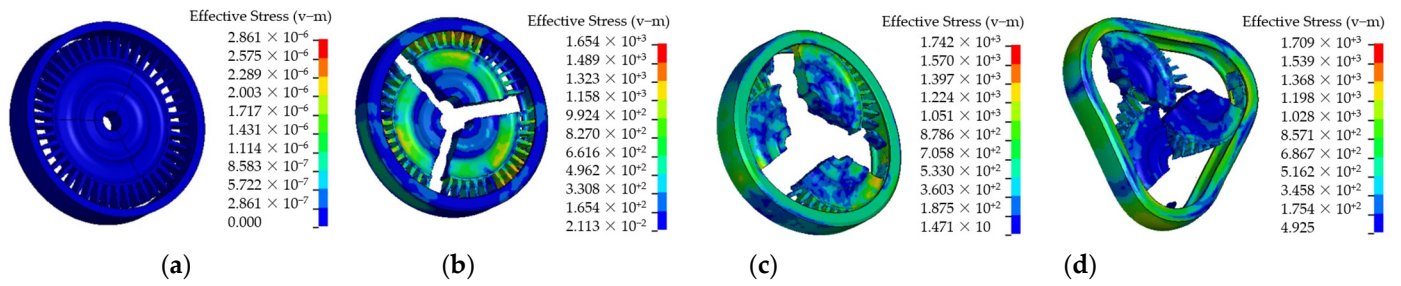


Figure 16. Process of the turbine wheel pieces impacting the containment ring with $T = 7.8$ mm. (a) $t = 0$ ms; (b) $t = 0.09$ ms; (c) $t = 0.30$ ms; (d) $t = 0.50$ ms.

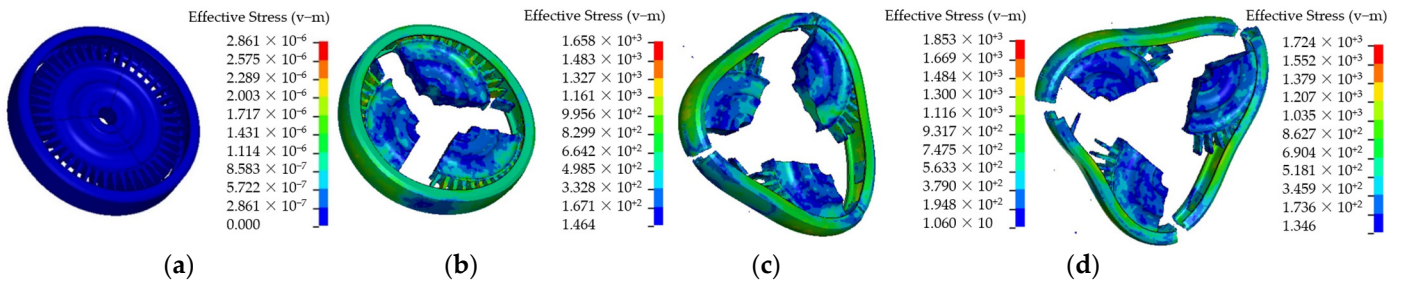


Figure 17. Process of the turbine wheel pieces impacting the containment ring with $T = 7.6$ mm. (a) $t = 0$ ms; (b) $t = 0.09$ ms; (c) $t = 0.15$ ms; (d) $t = 0.27$ ms.

4.4. Containment Simulation for the Rim Burst

The impact processes of the trisection, quarter and quintile rim burst are similar with that of the trisection wheel burst. Table 9 is the containment simulation for the three rim burst modes. Table 9 shows that the containment rings fully deform plastically to be the triangle, quadrangle and pentagon for the trisection, quarter and quintile rim burst, respectively. The containment rings with comparative thicknesses break, because their absorbed energy is less than the impact energy of the wheel rim pieces. The simulation results illustrate that $T = 5.5$, 5 and 4 mm are the critical thicknesses of the containment rings for the trisection, quarter and quintile rim burst.

Table 9. Containment simulation for three rim burst modes.

Burst Modes	Trisection Rim Burst	Quarter Rim Burst	Quintile Rim Burst
Critical thickness	<p>(a) $T = 5.5$ mm</p>	<p>(b) $T = 5$ mm</p>	<p>(c) $T = 4$ mm</p>
	<p>(d) $T = 5.3$ mm</p>	<p>(e) $T = 4.8$ mm</p>	<p>(f) $T = 3.8$ mm</p>
Thickness for comparison			

4.5. Comparison between Different Burst Modes

The simulation results for different burst modes with the critical thicknesses are compared. Figure 18 is the comparison of the initial kinetic energy of pieces for different burst modes. Figure 18 shows that compared with the trisection wheel burst (60.2 kJ), the initial kinetic energy of pieces for rim burst (45.3 kJ) decreases dramatically by 24.8%. Figure 19 is the comparison of the critical thickness of the containment ring for different burst modes. Figure 19 shows that compared with the trisection wheel burst (7.8 mm), the critical thicknesses of the containment ring for the trisection, quarter and quintile rim burst (5.5, 4.5 and 4.0 mm) decrease dramatically by 29.5%, 42.3% and 48.7%, respectively. Figure 19 also shows that for the rim burst modes, the more pieces the wheel rim breaks, the smaller the critical thickness of the containment ring is. The simulation results from Figs. 18 and 19 mean that compared with the wheel burst, the rim burst can dramatically decrease the initial kinetic energy of pieces and the critical thickness of the containment ring, and thereby reduce the mass of the containment ring.

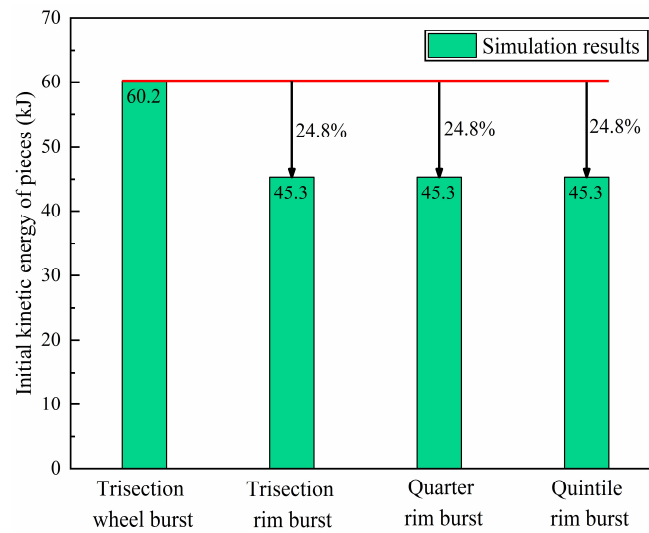


Figure 18. Comparison of the initial kinetic energy of pieces for different burst modes.

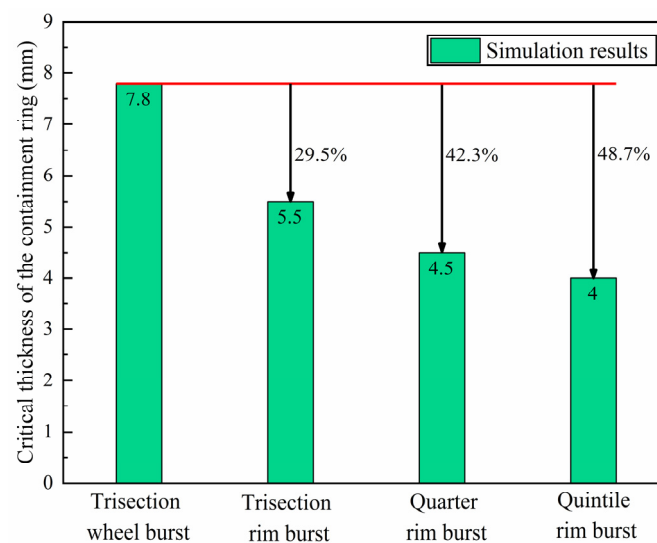


Figure 19. Comparison of the critical thickness of the containment ring for different burst modes.

Figure 20 is the comparison of the change rate of the containment ring diameter for different burst modes. Figure 20 shows that the change rates of the containment ring diameter for all burst modes are larger than 13.0%, which means that the containment

rings are fully deformed. Figure 20 also shows that the change rates of the containment ring diameter for the trisection, quarter and quintile rim burst are 13.1%, 14.0% and 14.9%, respectively. It means that the change rate of the containment ring diameter increases with the increase of the number of the wheel rim pieces.

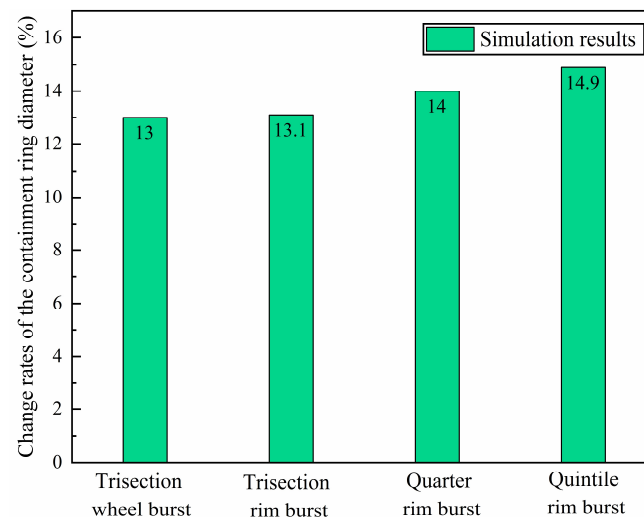


Figure 20. Comparison of the change rate of the containment ring diameter for different burst modes.

5. Experimental Verification of the Containment for Different Turbine Wheel Burst Modes

To verify the simulation results of Section 4, two and three containment tests were conducted for the trisection wheel burst and rim burst, respectively. In the condition of the clutch disconnect failure, the air turbine starter is driven in reverse by the aeroengine and the experience operation at a higher speed (larger than the turbine free run speed). It leads to the failure of the support bearings, thus allowing the axial travel of the turbine wheel. The turbine rim cutter is located in the air turbine starter, and the axial travel of the turbine wheel results in contact between the turbine wheel and the turbine rim cutter. For the contact position of the turbine wheel, the temperature sharply rises. It leads to the rapid reduction of the material property, thereby realizing the rim burst. Therefore, heating the neck of the wheel is adopted for the rim burst containment test.

5.1. Turbine Wheel and Containment Ring

The practicality picture of the turbine wheel ($\lambda = 1.4$) and containment ring are shown in Figure 21. To ensure the trisection wheel burst, there are three radial slots in the turbine wheel as shown in Figure 21a. To ensure the rim burst at the target burst speed, the red zone in Figure 21b is heated by the induction coil during the test.

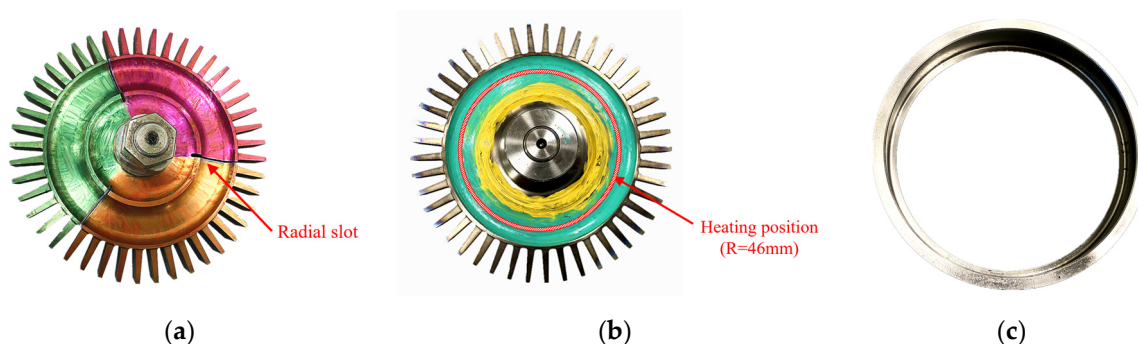


Figure 21. Practicality picture of the turbine wheel and containment ring. (a) Wheel for trisection wheel burst; (b) wheel for rim burst; (c) containment ring.

Five thicknesses of the containment ring are selected for containment tests as listed in Table 10. $T = 7.8$ and 7.6 mm are selected to verify the critical thickness of the containment ring for the trisection wheel burst. $T = 5.5$ and 4.0 mm are the critical thicknesses of the containment ring for the trisection and quintile rim burst, respectively. The number of wheel rim pieces is unknown before tests. To obtain the critical thickness of the containment ring for the rim burst, $T = 5.5$ and 4.0 mm are selected. $T = 3.8$ mm is selected for comparison.

Table 10. Five thicknesses of the containment ring for containment tests.

Burst Modes	Trisection Wheel Burst		Rim Burst		
T (mm)	7.8	7.6	5.5	4.0	3.8

5.2. Containment Test

The containment test and the rotor over-speed burst test adopted the same test bed, as shown in Figure 8. For the containment test of the trisection wheel burst, the containment ring is connected to the tester cavity cover through the mount base, as shown in Figure 22. For the containment test of the rim burst, the installation of the wheel and containment ring is similar to the containment test of the trisection wheel burst, and the induction coil is installed on the salver under the turbine wheel.

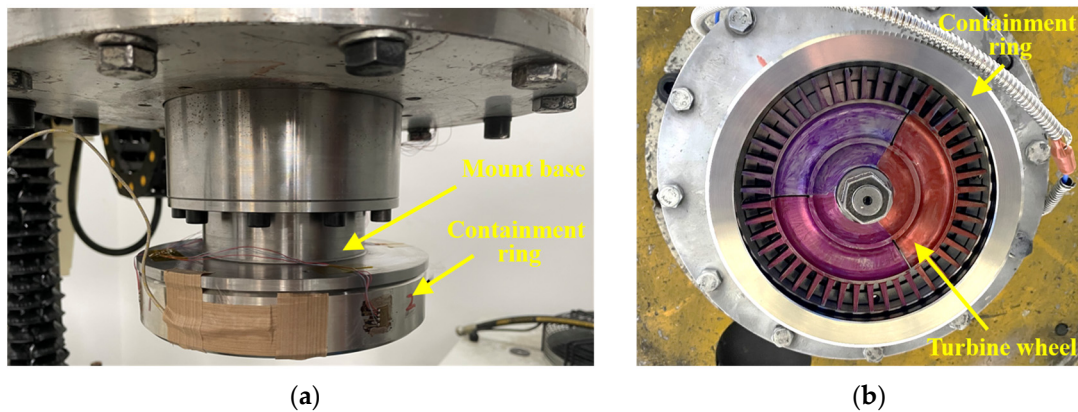


Figure 22. Containment test of the trisection wheel burst. (a) Front view; (b) bottom view.

5.3. Comparison with Experimental Results

Figure 23 is the burst speed for five containment tests. It shows that the errors of all burst speeds are less than 1%, which indicates the effectiveness of the experimental results.

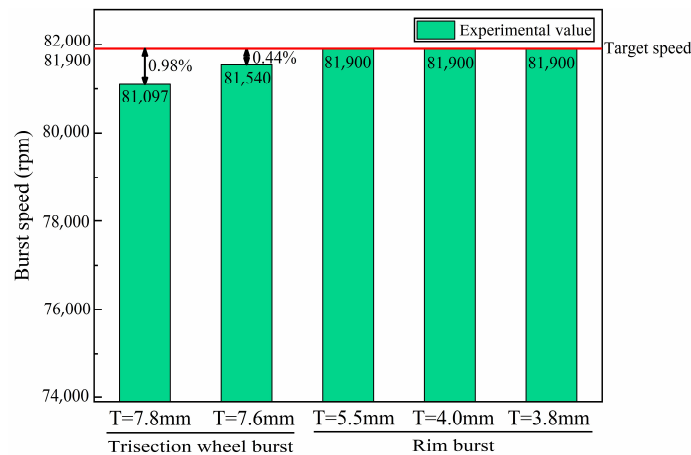


Figure 23. Burst speed for five containment tests.

Figure 24 is the process of the containment tests of the trisection wheel burst. Figure 24a shows that when $t = 0.10$ ms, the turbine wheel cracks into three pieces, which first contact the containment ring, and the containment ring starts to deform. When $t = 0.15$ ms, the containment ring deforms plastically to absorb the impact energy, and its shape tends to be triangular. When $t = 0.20$ ms, the turbine wheel pieces stop impacting the containment ring, and the containment ring fully deforms to be a triangle. Figure 24b shows that when $t = 0.10$ ms, the turbine wheel cracks into three pieces, which first contact the containment ring, and the containment ring starts to deform. When $t = 0.15$ ms, the containment ring fully deforms plastically to be a triangle. When $t = 0.20$ ms, the containment ring breaks. Figure 24 illustrates that $T = 7.8$ mm is the critical thickness of the containment ring for the trisection wheel burst. The experimental results are consistent with the simulation, verifying the accuracy of the simulation results.

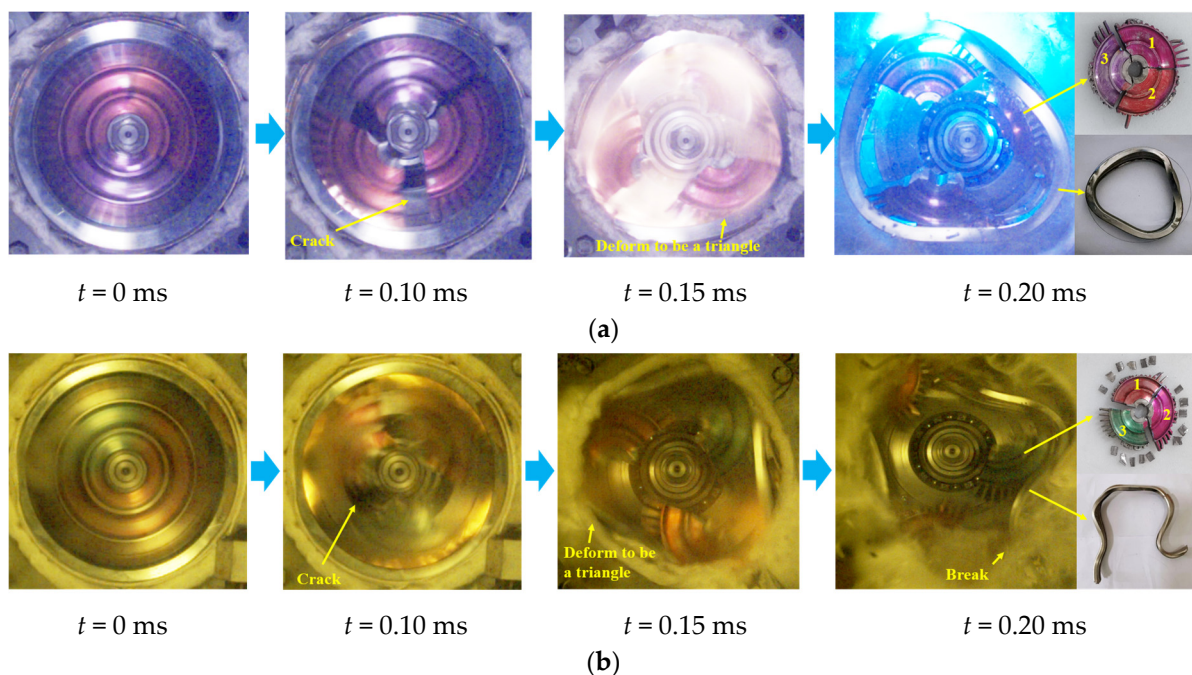


Figure 24. Process of the containment tests of the trisection wheel burst. (a) $T = 7.8$ mm; (b) $T = 7.6$ mm.

Figure 25 is the process of the containment tests of the rim burst. The containment test process of the rim burst for $T = 5.5$ mm (Figure 25a) is similar to that of the trisection wheel burst for $T = 7.8$ mm (Figure 24a). The containment test processes of the rim burst for $T = 4.0$ and 3.8 mm (Figure 25b,c) are similar with that of the trisection wheel burst for $T = 7.6$ mm (Figure 24b).

It should be noted that the deformed shape of the containment ring is related to the number of wheel rim pieces. Figure 25 shows that the deformed shapes of the containment rings are a quadrangle and pentagon for four and five rim pieces, respectively. The more rim pieces, the more fully the containment ring deforms, and the more energy the containment ring absorbs. Figure 25a shows that the containment ring with $T = 5.5$ mm does not break. The reason is that the rim breaks into five pieces, and $T = 5.5$ mm is the critical thickness for the trisection rim burst. It means that the energy absorption capacity of the containment ring with $T = 5.5$ mm is larger than the impact energy of the five rim pieces. Figure 25b shows that the containment ring with $T = 4.0$ mm breaks. The reason is that the rim breaks into four pieces, and $T = 4.0$ mm is the critical thickness for the quintile rim burst. It means that the energy absorption capacity of the containment ring with $T = 4.0$ mm is less than the impact energy of the four rim pieces. Figure 25c shows that the containment ring with $T = 3.8$ mm breaks, because $T = 3.8$ mm is less than the critical thickness for the quintile rim burst. The experimental results are consistent with the simulation, verifying the accuracy

of the simulation results. $T = 5.5$ mm should be adopted as the thickness of the containment ring for the rim burst, because the impact energy is at a maximum with the trisection rim burst in the case of the rim burst.

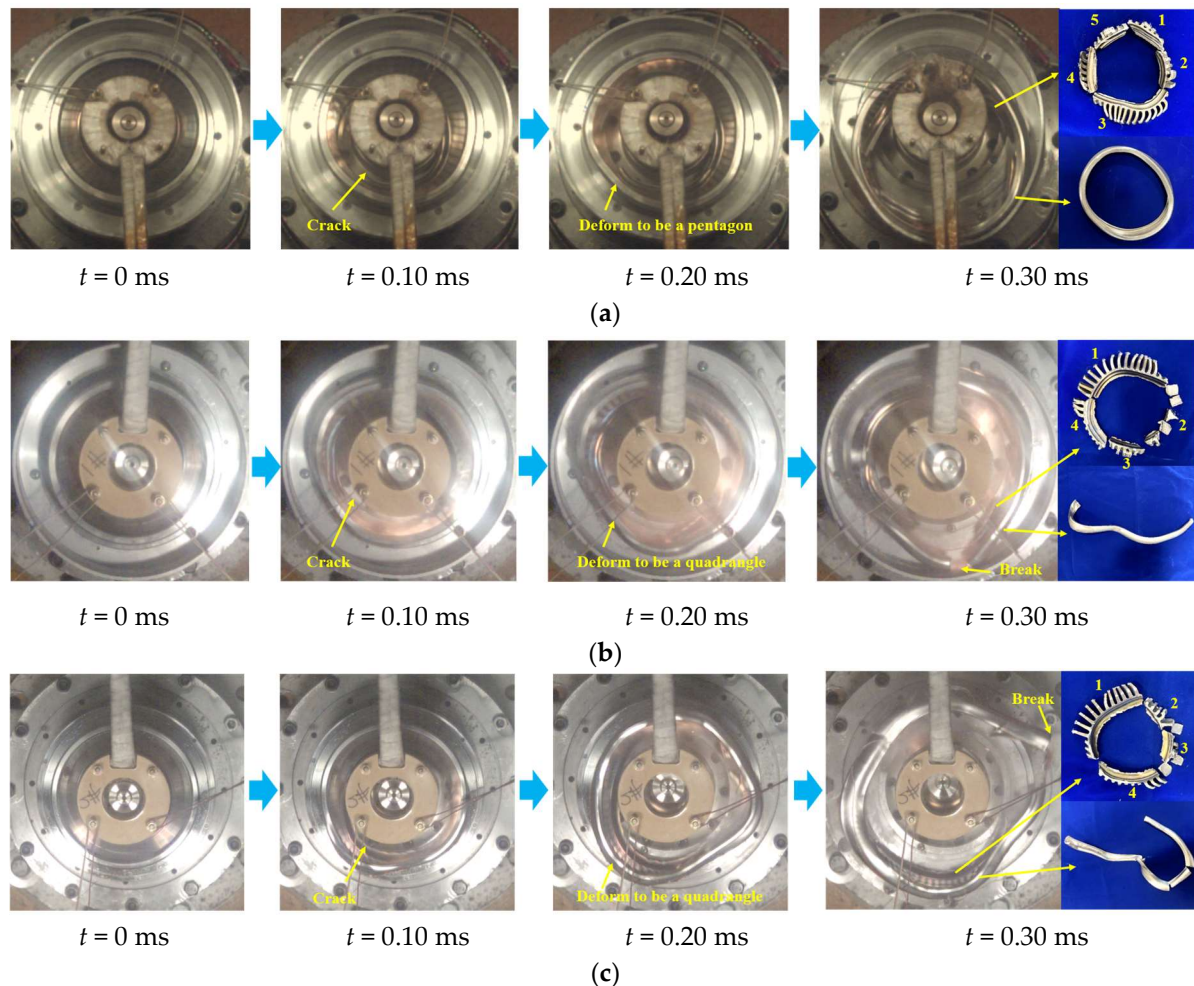


Figure 25. Process of the containment tests of the rim burst. (a) $T = 5.5$ mm; (b) $T = 4.0$ mm; (c) $T = 3.8$ mm.

Based on the experimental and simulation results, the containment design method is formed for the neck structure turbine wheel, and $T = 5.5$ mm is suggested as the design thickness of the containment ring. Figure 26 is a comparison of the burst piece masses and the containment ring masses between the trisection wheel burst (with $T = 7.8$) and the rim burst (with $T = 5.5$ mm). Figure 26 shows that compared with the trisection wheel piece, the masses of the rim pieces and the containment ring decrease by 63.3% and 29.1%, respectively. It means that the containment design method can greatly reduce the burst piece mass, and thereby reduce the containment ring mass.

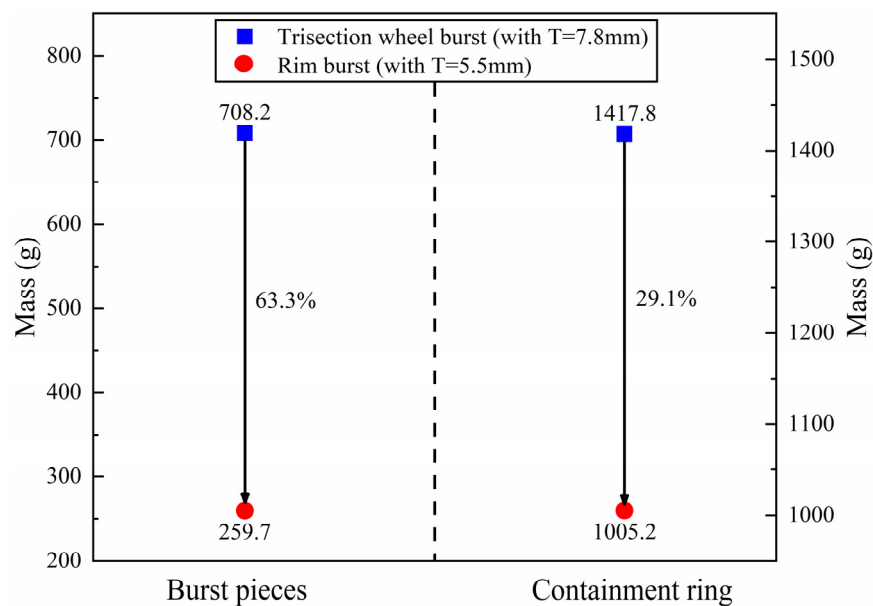


Figure 26. Comparison of the burst piece masses and the containment ring masses between the trisection wheel burst (with $T = 7.8$) and the rim burst (with $T = 5.5$ mm).

6. Conclusions

Based on an OSF design, Kriging response surface model and MOGA algorithm, a neck structure optimal design method was proposed for the turbine wheel, and verified by the rotor over-speed burst test. Then, the effect of turbine wheel burst modes on the containment was investigated quantitatively and verified by the containment tests of different burst modes. Based on the experimental and simulation results, the containment design method was proposed for the neck structure turbine wheel. Some key conclusions of this work can be summarized as follows:

- (1) Six structure parameters of the neck structure turbine wheel are optimized by the optimal design method, and the optimal structural parameters with the scaling factor $\lambda = 1.2, 1.3$ and 1.4 are obtained. The maximum errors of the burst speeds between the over-speed burst experimental and design values are less than 2%, and the neck structure turbine wheel breaks in the neck, validating the accuracy of the optimal design method proposed in this paper.
- (2) Compared with the trisection wheel burst (60.2 kJ), initial kinetic energy of pieces for rim burst (45.3 kJ) decreases dramatically by 24.8%. Compared with the trisection wheel burst (7.8 mm), the critical thicknesses of the containment ring for the trisection, quarter and quintile rim burst (5.5, 4.5 and 4.0 mm) decrease dramatically by 29.5%, 42.3% and 48.7%, respectively.
- (3) For the neck structure turbine wheel, the mass and initial kinetic energy of the rim pieces are 257.9 g and 45.3 kJ, respectively. Compared with the trisection wheel pieces, the mass and initial kinetic energy of the rim pieces decrease dramatically by 63.3% and 24.8%, respectively. As a result, the thickness and mass of the containment ring decrease greatly by 29.5% and 29.1%, respectively. Therefore, the neck structure turbine wheel can dramatically decrease the mass and initial kinetic energy of the burst pieces from the wheel, thereby reducing the thickness and mass of the containment ring.

It is worth noting that the neck structure optimal design of the turbine wheel was verified by the component containment test. The component containment test is only composed of the turbine wheel and containment ring. However, the working condition of the whole air turbine starter is more complicated than that of the component containment test. In future research, the containment test of the whole air turbine starter will be conducted to verify the optimal neck structure turbine wheel, and the experimental results can guide the containment design of the in-service air turbine starter.

To ensure the computational precision and efficiency, the neck structure optimal design method employed the OSF design, Kriging response surface model and MOGA algorithm. However, the YUKI algorithm [30] and Proper orthogonal Decomposition endorsed with Radial Basic Function (POD-RBF) [31] were also proven to be effective computational-wise and used in dynamic analysis. In the future research, the YUKI algorithm and POD-RBF will be employed to optimize the neck structure turbine wheel, and the computational precision and efficiency between different optimization methods will be compared.

Author Contributions: Conceptualization, L.C. and H.X.; methodology, H.X. and Y.Z.; software, W.J. and Z.F.; validation, H.X. and W.J.; formal analysis, W.J.; investigation, J.L.; data curation, W.J.; writing—original draft preparation, W.J., L.C., J.L. and Z.F.; writing—review and editing, H.X. and Y.Z.; visualization, W.J.; supervision, H.X. All authors have read and agreed to the published version of the manuscript.

Funding: This work was supported by the National Science and Technology Major Project (2017-IV-0006-0043).

Data Availability Statement: The data underlying the results presented in this paper are not publicly available at this time.

Conflicts of Interest: The authors declare no conflict of interest.

References

- Guo, R.X.; Liu, Z.H.; Wei, Y. Remaining useful life prediction for the air turbine starter based on empirical mode decomposition and relevance vector machine. *Trans. Inst. Meas. Control.* **2020**, *42*, 2578–2588. [\[CrossRef\]](#)
- SAE Aerospace. *Air Conditioning Systems for Subsonic Airplanes*; SAE Aerospace-ARP-85F; Society of Automotive Engineers (SAE) Aerospace: Warrendale, PA, USA, 2012; p. 27.
- Moussa, N.A.; Whale, M.D.; Grozmann, D.E.; Zhang, X.J. *The Potential for Fuel Tank Fire and Hydrodynamic Ram from Uncontained Aircraft Engine Debris*; Report No. DOT/FAA/AR-96/95; US Department of Transportation, Federal Aviation Administration: Washington, DC, USA, 1997.
- Australian Transport Safety Bureau. *Uncontained Engine Starter Failure-General Electric CF6-80E1-A3-Darwin Aerodrome*; Report No. AO-2007-052; Australian Transport Safety Bureau: Canberra, Australia, 2007.
- Australian Transport Safety Bureau. *In-Flight Engine Shut down Involving Airbus A330-302 B-18358*; Report No. AO-2013-172; Australian Transport Safety Bureau: Canberra, Australia, 2013.
- Civil Aviation Safety Authority. Airworthiness directive, Civil Aviation Safety Regulations Part39-106. In *Schedule of Airworthiness Directives*; Civil Aviation Safety Authority: Canberra, Australia, 2007.
- AA Federal Aviation Regulations. *Airworthiness Standards: Aircraft Engines*; Federal Aviation Administration: Washington, DC, USA, 1984.
- Civil Aviation Administration of China. *CARR-25-R4 Airworthiness Standards for Transport Aircraft*; Civil Aviation Administration of China: Beijing, China, 2011.
- Martino, A.A.; Mangano, G.J. *Rotor Burst Protection Program Initial Test Results*; NASA DPR R-105; Naval Air Propulsion Test Center, Aeronautical Engine Department: Philadelphia, PA, USA, 1968.
- Mccallum, R.B. Simplified analysis of a trisegment rotor disk interaction with a containment ring. *J. Aircr.* **1970**, *7*, 283–285. [\[CrossRef\]](#)
- Collins, T.P.; Witmer, E.A. *Application of the Collision-Imparted Velocity Method for Analyzing the Responses of Containment and Deflector Structures to Engine Rotor Fragment Impact*; NASA CR-134494; Aeroelastic and Structure Research Laboratory, Department of Aeronautics and Astronautics, Massachusetts Institute of Technology: Cambridge, MA, USA, 1973.
- Hagg, A.C.; Sankey, G.O. The containment of disk burst fragments by cylindrical shells. *J. Eng. Power* **1974**, *96*, 114–123. [\[CrossRef\]](#)
- Gerstle, J.H. Analysis of rotor fragment impact on ballistic fabric engine burst containment shields. *J. Aircr.* **1975**, *12*, 388–393. [\[CrossRef\]](#)
- Giard, J.R. Air Turbine Starter Turbine Wheel Containment. *SAE Trans.* **1984**, *93*, 459–463.
- Frankenberger, C.E., III. *FAA T53-L13L Turbine Fragment Containment Test*; Report No. DOT/FAA/AR-98/22; U.S. Department of Transportation, Federal Aviation Administration: Washington, DC, USA, 1998.
- Teng, X.; Wierzbicki, T. Gouging and fracture of engine containment structure under fragment impact. *J. Aerosp. Eng.* **2008**, *21*, 174–186. [\[CrossRef\]](#)
- Stamper, E.; Hale, S. The use of LS-DYNA models to predict containment of disk burst fragments. In Proceedings of the 10th International LS-DYNA User Conference, Dearborn, MI, USA, 1–9 January 2008.
- Carney, K.S.; Pereira, J.M.; Revilock, D.M.; Matheny, P. Jet engine fan blade containment using an alternate geometry. *Int. J. Impact Eng.* **2009**, *36*, 720–728. [\[CrossRef\]](#)

19. Li, J.J.; Xuan, H.J.; Liao, L.F.; Hong, W.R.; Wu, R.R. Penetration of disk fragments following impact on thin plate. *J. Zhejiang Univ. Sci. A* **2009**, *10*, 677–684. [[CrossRef](#)]
20. Xuan, H.J.; Liu, L.L.; Feng, Y.M.; He, Q.; Li, J.J. Containment of high-speed rotating disk fragments. *J. Zhejiang Univ. Sci. A* **2012**, *13*, 665–673. [[CrossRef](#)]
21. Winter, T.; Hu, A.; Beck, H. Simulation of Containment-Tests of Fast-Spinning Rotors by Explicit FEM. Available online: <https://www.dynalook.com/conferences/european-conf-2007/simulation-of-containment-tests-of-fast-spinning.pdf> (accessed on 14 August 2023).
22. Bai, C.E.; Xuan, H.J.; Huang, X.N.; He, Z.; Hong, W. Containment ability and groove depth design of U type protection ring. *Chin. J. Aeronaut* **2016**, *29*, 395–402. [[CrossRef](#)]
23. Wang, X.; Tsung, F.; Li, W.; Xiang, D.; Cheng, C. Optimal space-filling design for symmetrical global sensitivity analysis of complex black-box models. *Appl. Math. Model.* **2021**, *100*, 303–319. [[CrossRef](#)]
24. Wang, Y.; Pan, H.; Shi, Y.; Wang, R.; Wang, P. A new active-learning estimation method for the failure probability of structural reliability based on Kriging model and simple penalty function. *Comput. Methods Appl. Mech. Eng.* **2023**, *410*, 116035.
25. Haftka, R.T.; Villanueva, D.; Chaudhuri, A. Parallel surrogate assisted global optimization with expensive functions a survey. *Struct. Multidiscip. Optim.* **2016**, *54*, 3–13. [[CrossRef](#)]
26. Srinivas, N.; Deb, K. Multi-objective function optimization using non-dominated sorting genetic algorithms. *Evol. Comput.* **1994**, *2*, 1301–1308. [[CrossRef](#)]
27. Johnson, G.R.; Cook, W.H. A constitutive model and data for metals subjected to large strains, high rates and high temperatures. In Proceedings of the 7th International Symposium on Ballistics, Hague, The Netherlands, 19–21 April 1983; pp. 541–557.
28. Johnson, G.R.; Cook, W.H. Fracture characteristics of three metals subjected to various strains, strain rates, temperatures and pressures. *Eng. Fract. Mech.* **1985**, *21*, 31–48. [[CrossRef](#)]
29. He, Z.; Xuan, H.; Bai, C.; Song, M.; Zhu, Z. Containment of soft wall casing wrapped with Kevlar fabric. *Chin. J. Aeronaut* **2019**, *32*, 954–966. [[CrossRef](#)]
30. Benaissa, B.; Hocine, N.A.; Khatir, S.; Riahi, M.K.; Mirjalili, S. YUKI Algorithm and POD-RBF for Elastostatic and dynamic crack identification. *J. Comput. Sci.* **2021**, *55*, 101451. [[CrossRef](#)]
31. Buljak, V.; Maier, G. Proper orthogonal decomposition and radial basis functions in material characterization based on instrumented indentation. *Eng. Struct.* **2011**, *33*, 492–501. [[CrossRef](#)]

Disclaimer/Publisher’s Note: The statements, opinions and data contained in all publications are solely those of the individual author(s) and contributor(s) and not of MDPI and/or the editor(s). MDPI and/or the editor(s) disclaim responsibility for any injury to people or property resulting from any ideas, methods, instructions or products referred to in the content.